Representation of tropical subseasonal variability of precipitation in global reanalyses

Daehyun Kim[1], Myong-In Lee[2], Dongmin Kim[2], Siegfried D. Schubert[3], Duane E. Waliser[4], and Baijun Tian[4]

[1]Lamont-Doherty Earth Observatory, Columbia University, Palisades, NY, U.S.A.

[2]Ulsan National Institute of Science and Technology, Ulsan, Korea

[3]NASA Goddard Space Flight Center, MD, U.S.A.

[4]NASA Jet Propulsion Laboratory, CA, U.S.A.

July 2013

(revised)

Corresponding author address: Myong-In Lee, School of Urban and Environmental Engineering, Ulsan National Institute of Science and Technology, UNIST-gil 50, Ulsan 689-798, Republic of Korea, e-mail: milee@unist.ac.kr

Abstract

Tropical subseasonal variability of precipitation from five global reanalyses (RAs) is evaluated against Global Precipitation Climatology Project (GPCP) and Tropical Rainfall Measuring Mission (TRMM) observations. The RAs include the three generations of global RAs from the National Center for Environmental Prediction (NCEP), and two other RAs from the European Centre for Medium-Range Weather Forecasts (ECMWF) and the National Aeronautics and Space Administration/Goddard Space Flight Center (NASA/GSFC). The analysis includes comparisons of the seasonal means and subseasonal variances of precipitation, and probability densities of rain intensity in selected areas. In addition, the space-time power spectrum was computed to examine the tropical Madden-Julian Oscillation (MJO) and convectively coupled equatorial waves (CCEWs).

The modern RAs show significant improvement in their representation of the mean state and subseasonal variability of precipitation when compared to the two older NCEP RAs: patterns of the seasonal mean state and the amplitude of subseasonal variability are more realistic in the modern RAs. However, the probability density of rain intensity in the modern RAs show discrepancies from observations that are similar to what the old RAs have. The modern RAs show higher coherence of CCEWs with observed variability and more realistic eastward propagation of the MJO precipitation. The modern RAs, however, exhibit common systematic deficiencies including: i) variability of the CCEWs that tends to be either too weak or too strong, ii) limited coherence with observations for waves other than the MJO, and iii) a systematic phase lead or lag for the higher-frequency waves.

Key Words: reanalysis, precipitation, tropics, subseasonal variability, Madden-Julian oscillation, convectively-coupled equatorial waves

1. Introduction

Global atmospheric reanalysis products (RAs) have been widely used in scientific research and applications, and they are now invaluable resources for weather and climate studies. Providing dynamically- and physically-consistent global atmospheric states, that are contiously constrained by observations in time and space, RAs have helped to enlarge our understanding of climate and its low-frequency variability. Since the first global, multi-decadal RA was produced by the National Center for Environmental Prediction and National Center for Atmospheric Research (NCEP/NCAR, Kalnay et al. 1996), the number of variables, time frequency, spatial resolution, and the analysis period have substantially increased. Examples include the NCEP-Department of Energy reanalysis (NCEP-DOE, Kanamitsu et al. 2002), the 40-year European Centre for Medium-Range Weather Forecast (ECMWF) reanalysis (ERA-40, Uppala et al. 2005), and the Japanese 25-year reanalysis (JRA-25, Onogi et al. 2007). The data quality has been improved significantly as well, by virtue of increased observational data over the globe, and improved global forecast models and data assimilation techniques. This has led to the production of the most recent RAs: the NCEP Climate Forecast System Reanalysis (CSFR, Saha et al. 2010), the ERA-interim Reanalysis (ERA-I, Dee et al. 2011), NASA's Modern-Era Retrospective Analysis for Research and Applications (MERRA, Rienecker et al. 2011), and the NOAA-CIRES Twentieth Century Reanalysis (20CR, Compo et al., 2011).

With these multiple modern RAs, it is now possible to objectively identify the common and discriminating features across RAs, as well as assessing improvements from the older RAs - a major focus of this study. Previous studies have already shown that there are substantial differences among the RAs. For example, Hodge et al. (2011) showed that the differences among RAs in their representation of mid-latitude storms were large and systematic. Another typical example is the representation of the tropical Madden-Julian Oscillation (MJO) and associated subseasonal variability, where the convective signal and precipitation in RAs are only weakly constrained by observations that are less frequent and larger scale than the typical characteristic time and space scale of tropical deep convection. Indeed, the representation of the tropical subseasonal variability hinges on the individual assimilation system, observation sources, and the parameterized moist physics in the global forecast model. This study focuses on examining the capability of RAs in representing the MJO and the associated subseasonal variability in precipitation in the tropics. Although atmospheric moisture content and precipitation[1] are assimilated in the modern RAs, the representation of clouds and precipitation is still significantly affected by errors in the parameterizations of cloud processes. It is often assumed that wind fields from RAs are more reliable than the precipitation. The winds are, however, tightly coupled to precipitation through dynamical balances especially over the tropical ocean where in-situ observations are

[1] Precipitation is assimilated only in ERA-I and MERRA.

sparse. Therefore, one need to be aware of the quality and uncertainty of RA precipitation even when he works with wind data.

Tropical subseasonal variability occurs on various space and time scales. Mesoscale convective systems are often embedded in equatorially trapped waves referred to as convectively coupled equatorial waves (CCEWs). These CCEWs account for a significant portion of the subseasonal variability of precipitation. By modulating tropical deep convection, CCEWs have large impacts on a wide variety of climate phenomena across different spatial and temporal scales. Some examples include the onset and break of the Indian and Australian summer monsoons (e.g. Yasunari 1979; Wheeler and McBride 2005), the formation of tropical cyclones (e.g. Liebmann et al. 1994; Maloney and Hartmann 2000a; Maloney and Hartmann 2000b; Bessafi and Wheeler 2006; Frank and Roundy 2006; Molinari et al. 2007) and the onset of some El Nino events (e.g. Takayabu et al. 1999; Bergman et al. 2001; Kessler 2001). For a more thorough review on the impacts of the CCEWs, the reader is referred to Kiladis et al. (2009) and Zhang et al. (2005). Clearly, RAs need to correctly represent CCEWs if they are to be used to study almost any aspects of tropical subseasonal variability.

Among the CCEWs, the Madden-Julian oscillation (MJO, Madden and Julian 1972) is the dominant mode of tropical subseasonal variability, characterized by planetary wavenumbers 1-3, a low-frequency period of 30-60 days, and prominent eastward propagation. Despite its importance, our level of understanding of the dynamics of the

MJO is still incomplete. For example, there is no single generally accepted theory for the MJO, though a number of theories have been suggested (see e.g., Zhang 2005 and Wang 2005, 2011; Majda and Stechmann, 2011). This is reflected in generally poor simulations of the MJO with state-of-the-art general circulation models (GCMs) (e.g. Lin et al. 2006; Kim et al. 2009; Hung et al. 2013, Sperber et al. 2011).

With the exception of the MJO, the existence of CCEWs was predicted by a theoretical study of Matsuno (1966). Matsuno solved the shallow-water equations on an equatorial beta-plane and obtained solutions of the various equatorially trapped waves, including: the Kelvin wave, the n=1 westward inertia-gravity wave, the mixed Rossby-gravity wave, the n=0 eastward inertia-gravity wave, and the Equatorial Rossby wave. Subsequent analysis of long-term, global satellite data revealed the signature of these waves in the variability of tropical deep convection (Takayabu 1994; Wheeler and Kiladis 1999). Further studies have revealed the structure of the waves using the global RAs (e.g., Sperber 2003; Yang et al. 2007), but our understanding of these waves, especially the interaction between moist convection and atmospheric circulations is still limited (Kiladis et al. 2009).

Given the limited number of observations in the tropics, global RAs are our best choice for studying CCEWs. Unfortunately, there is currently very limited information about the quality of the RAs in representing CCEWs, while several studies examined CCEWs simulated in GCMs (Lin et al. 2006; Frierson et al. 2011; Hung et al. 2013). We aim to provide such information through a detailed evaluation of the RAs' precipitation.

The paper is organized as follows. Section 2 describes the RAs and observations used in this study. The mean state and subseasonal variability of precipitation during boreal winter and summer are evaluated in Section 3. A wavenumber-frequency analysis is presented in Section 4. The summary and conclusions are given in Section 5.

2. The Reanalyses and Observations

The key observational dataset used in this study is version 1.1 of the Global Precipitation Climatology Project (GPCP) daily precipitation data (Huffman et al. 2001). The original 1^{o} x 1^{o} latitude-longitude data were interpolated onto a 2.5^{o} x 2.5^{o} grid. The Tropical Rainfall Measuring Mission (TRMM) 3B42 version 6 daily precipitation data (Huffman et al. 2007) is also used to address the uncertainty in the observed precipitation. Note that both products use 3-hourly global infrared brightness temperature maps to create daily-mean precipitation estimates. We restrict our analysis period to 1997-2008 (1998-2008 for TRMM), because GPCP data is available after 1 January 1997, and we think more than 10 years of daily data is enough for an evaluation of the subseasonal variability.

Table 1 summarizes the five RAs to be compared in this study. For a full description of each RA the interested readers may refer to the papers listed in the table. Here we only describe a few features relevant to our discussion. The horizontal resolution of the global atmospheric models used in the data assimilation systems ranges from 32 to 200 km, where the T62 (~ 200 km) of NCEP/NCAR and NCEP-DOE is the lowest and the T382 (~ 38 km) of NCEP CFSR is the highest. The number of vertical levels also varies across the RAs, with 28 levels in NCEP/NCAR and NCEP-DOE, and more than 60 levels in CFSR (64), ERA-I (72), and MERRA (72 – this is the number of model levels) . Since most of RAs examined in this study except ERA-I and MERRA do not use the observed rainfall in the assimilation process[2], the moist physics of the global model including the deep convective parameterization plays an important role in dictating the spatial and temporal variability of precipitation in the tropics. All the RAs use local buoyancy-based, mass-flux convection schemes, although the details of the closure assumption and convection triggering process are quite different across the global forecast models (Moorthi and Suarez, 1992; Pan and Wu, 1994; Hong and Pan, 1998; Bechtold et al. 2001). Regarding the assimilation technique, CFSR, ERA-I, and MERRA use techniques that performs in four-dimensional space. This enables the techniques to consider observations at the future times with respect to the target analysis time. The influence of the observations during the course of the assimilation occurs through, a first-order time interpolation scheme (Rancic et al. 2008), the four-dimensional variational assimilation technique, and the incremental analysis update scheme (Bloom et al, 1996) in CFSR, ERA-I, and MERRA, respectively. Daily-averaged RA precipitation was created using 6-

[2] When MERRA assimilates precipitation observation over oceans, it is weighted only very weakly so that it effectively has almost no impact.

hourly datasets except for MERRA, where 3-hourly data was used. For this study, all the precipitation data were spatially interpolated onto the same 2.5°x2.5° latitude-longitude grid.

The quality of RA precipitation is affected significantly by the quality of tropospheric moisture analysis. In RAs, tropospheric moisture is constrained by data from various observational systems including radiosondes, air-borne sensors, and satellites, among which satellite radiances are the dominant source of moisture information over the tropical oceans. This suggests that the availability of satellite radiances will have a strong impact on the quality of the RA precipitation products. The list of satellites and the instruments used to retrieve atmospheric humidity (vertical profile or column-integrated) are given in Table 2. Also indicated in Table 2 is the use of these data in the five RAs. Note that in the earlier RAs (NCEP/NCAR, NCEP-DOE) satellite-based moisture observations were not used. On the other hand, all the modern RAs (CFSR, ERA-I, and MERRA) incorporate satellite-based moisture data. For more details about the usage of these data, readers are referred to Figure 4 in Saha et al. (2010), Figure 14 in Dee et al. (2011), and Table B3 in Rienecker et al. (2011).

3. Results

a) Mean state

Kim et al. (2009) found that the quality of the spatial structure of the time-mean precipitation is closely linked to the capability to simulate the MJO among other variables, so we begin this section by presenting the time mean precipitation patterns.

Figures 1 and 2 show the time-mean precipitation from the RAs and observations during boreal winter (November-April) and summer (May-October), respectively. The pattern correlations and normalized amplitudes against GPCP of the seasonal mean precipitation maps in the RAs and TRMM are shown in Figure 3 in a Taylor diagram (Taylor 2001). Note that the two observational estimates – GPCP and TRMM are similar to each other. The observed magnitude of the mean precipitation is well captured in NCEP/NCAR, ERA-I, and MERRA, while NCEP-DOE and CFSR tend to overestimate it (Fig. 3). Overall, the modern RAs exhibit an improved pattern compared to the old RAs. Regional biases in RAs over the inter-tropical convergence zone (ITCZ) and the south Pacific convergence zone (SPCZ) can be also identified in the comparison. During boreal winter over the eastern Pacific (Fig. 1), all RAs exhibit stronger ITCZs in the southern hemisphere, although this is very weak in the GPCP and TRMM observation. In the older RAs (NCEP-NCAR and NCEP-DOE), this double-ITCZ pattern is also prominent during boreal summer (Fig.2). The SPCZ in boreal winter (Fig.1) is well captured in all products, while the peak of precipitation in the SPCZ is somewhat shifted to the east in NCEP/NCAR and NCEP-DOE, compared to the observations and other RAs. During boreal summer (Fig. 2), the RAs capture the rain bands related to the south Asian and western Pacific monsoons.

In the maritime continent, the GPCP and TRMM observation show rainfall maxima over the big islands with elevated topography (e.g., Borneo and New Guinea), and relatively smaller mean rainfall in the adjacent oceanic areas. This feature is seen in both seasons, but is particularly recognizable during boreal winter. This distribution of mean rainfall over the maritime continent is well captured in the modern RAs, and is represented with lesser realism in NCEP/NCAR and NCEP-DOE. The precipitation around the islands over the maritime continent is underestimated in NCEP/NCAR, and the minimum around 130^{o}E is not captured in NCEP-DOE. The increased horizontal resolution of the modern RAs (see Table 1) is obviously one factor that might have led to the improved representation over the maritime continent.

b) Probability density of rain intensity

Another statistics that provide useful information is the frequency of rain intensity. When the RAs reproduce time mean value of precipitation in a location, they are expected to do it with the right distribution of rain intensity values. It could be, however, from a different distribution of rain intensity values. For example, it is possible that a RA with too-frequent light rain events reproduces an observed mean value, which is a result of a few heavy precipitation events. Such mismatches could be illustrative of differences in underlying storm type(s), vertical distributions of latent heat, etc., and users of the RA products need to be aware of these characteristics. The probability density of rain rates in observations and RAs is shown in Figure 4. Fifty-one precipitation bins are used in the calculation of the probability density following Eq. (1), where lower (P_i^L) and upper (P_i^U) bounds of each (i-th) bin is defined.

$$P_i^L = 0, P_i^U = 0.09797, for\ i = 1$$
$$P_i^L = P_{i-1}^U, log_{10}P_i^U - log_{10}P_i^L = 0.065, for\ i = 2, 3, \cdots, 50 \quad (1)$$
$$P_i^L = 150, P_i^U = 1000, for\ i = 51$$

The probability density of rain rate is obtained using daily rain rates over the three areas: the Indo-Pacific Warm Pool (40-180°E, 20°S-20°N), the ITCZ (182.5-280°E, 2.5-10°N), and the southeastern Pacific (220-280°E, 2.5-10°S). The warm pool and ITCZ areas are where mean precipitation is higher than surrounding areas. It is therefore of interest whether the RAs produce mean rainfall in these areas with similar statistics of intensity of rain events to those in observations. The southeastern Pacific area is an area dominated by low mean precipitation and where some RAs exhibit the double ITCZ bias (Figs. 1 and 2). Probability density of rain events might provide insights on the physical nature of the bias.

Overall, GPCP and TRMM show a good agreement in all three areas, and the difference between the two observational estimates is smaller than the difference between those and RAs. Nonetheless, a systematic difference between GPCP and TRMM is notable. In the warm pool and ITCZ areas, GPCP has the probability of weak rain rate (< 10 mm day^{-1}) lower than that in TRMM, while GPCP shows a higher probability density of the strong rain event (> 10 mm day^{-1}) than that in TRMM. The frequency of weak rain event in TRMM is also higher than that in GPCP in the southeastern Pacific area. It should be noted that both GPCP and TRMM could have a systematic bias in the light-rain regime, due to the lack of sensitivity of IR-based sensors to warm rain events (Behrangi et al. 2012).

In the warm pool and ITCZ area, all RAs tend to overestimate the frequency of rain rates whose magnitude is near 10 mm day^{-1}. This is especially true in NCEP/NCAR, ERA-I, and MERRA. The RAs that overestimate these intermediate-intensity rain events underestimate the frequency of strong rain events. NCEP-DOE and CFSR exhibit relatively better statistics of the frequency of strong rain events. The probability density of strong rain events in those RAs is similar to those in GPCP and TRMM. MERRA has a peak near 1 mm day^{-1} rain rate in all areas considered, which is not seen in other RAs and observations. This suggests that the too-frequent light rain is an inherent feature of MERRA. Over the southeastern Pacific area, compared to the statistics over the warm pool and ITCZ areas, strong rain events are hardly observed in GPCP and TRMM. In this area, the RAs that have relatively larger time-mean double ITCZ bias (i.e. NCEP-NCAR and NCEP-DOE), overestimate the frequency of intermediate-to-strong rain events. In NCEP-NCAR, the frequency of the intermediate (1-10 mm day^{-1}) rain events is higher than the observed estimates, while NCEP-DOE overestimates the frequency of the strong (> 10 mm day^{-1}) rain events. On the contrary, the modern RAs overestimates the probability density of weak (< 1 mm day^{-1}) rain events. This suggests that the similar bias in the time-mean pattern in different RAs originates from a different physical nature. There is no systematic difference between the old and modern RAs in Figure 4.

c) Subseasonal variability

Subseasonal (20-100 day) variability accounts for a significant amount of the total variance in many tropical areas. Figure 5 and 6 display the variance of 20-100 day band-pass filtered precipitation during boreal winter and summer, respectively. The pattern correlation with that of GPCP and relative amplitude to that of GPCP is shown in Figure 7. Again, the two observations agree quite well, and the difference between GPCP and TRMM is much smaller than that between RAs and observations (Fig. 7), implying the observational uncertainty is smaller than errors in RAs.

The distribution of the subseasonal variability resembles that of the time-mean precipitation in general, but with a notable difference over land. In the observations during boreal winter (Figure 5), subseasonal variability has a minimum in the big islands over the maritime continent, whereas the seasonal-mean precipitation peaks there. During boreal summer (Figure 6), subseasonal variability in the Amazon and central Africa is much smaller than that over the Indian Ocean and the west Pacific, although mean precipitation is comparable in all these areas. This suggests that the time-mean precipitation over land and its time variance is also composed of shorter time scale phenomena such as diurnal convection (e.g. Tian et al. 2006) and other transients.

Sobel et al. (2008) suggested that the disagreement in relative magnitudes of time-mean precipitation and subseasonal variability over land is evidence of the importance of surface heat flux in driving subseasonal rainfall anomalies. That is, surface temperature and accompanying surface turbulent heat flux cannot generate low-frequency variability over land due to the negligible heat capacity there, consistent with the lack of subseasonal variability of precipitation over land. In all the RAs, this feature is well captured (Figs. 5 and 6), implying that the RAs are successfully segregating the subseasonal, low-frequency variability over ocean and relatively higher-frequency variability over land. The simulated amplitude of subseasonal variability over land (especially the islands over the maritime continent) is smaller than that over the oceanic area with comparable time-mean precipitation.

There are however large differences in the magnitude of precipitation variance in RAs, where NCEP-DOE and CFSR overestimate the variance and others underestimate it (Fig. 7). In Figure 8, we examine the ratio of the subseasonal (20-100 day) precipitation variance to the total variance. Here the total variance is defined as the squared averages of daily precipitation anomalies. In NCEP/NCAR, ERA-I, and MERRA, the fraction of rainfall variability explained by the subseasonal component is greater than that of observations (Fig. 8), although the overall subseasonal variability is underestimated (Fig. 7). NCEP-DOE and CFSR show stronger subseasonal variability than observed with comparable ratios of subseasonal to total variability (Fig. 8). This indicates that NCEP/NCAR, ERA-I, and MERRA tend to produce weaker precipitation variance in the shorter-time scales (less than 20 days), compared with observations.

The relationship between time-mean precipitation and the subseasonal precipitation variance is illustrated in Fig. 9, in terms of a scatter diagram between tropics (0-360°E, 30°S-30°N)–averaged standard deviation of subseasonal precipitation anomaly and the tropics time-mean precipitation. Relative to GPCP; NCEP/NCAR, ERA-I, and MERRA underestimate the subseasonal variability, while NCEP-DOE and CFSR overestimate it. Among the RAs, the magnitudes of the mean and subseasonal variability in the tropics show a monotonic relationship in which amplitude of subseasonal variability is expected to be high when the time-mean precipitation is high. The RAs, however, have a systematic wet bias compared to GPCP and TRMM.

d) A wavenumber-frequency analysis

In this subsection, we describe our analysis of the subseasonal variability of RA precipitation in zonal wavenumber and frequency space. First, the daily precipitation anomalies at latitude bands between 15°S and 15°N were separated into symmetric and antisymmetric components, following the method of Hendon and Wheeler (2008). For each component, a total of 83 segments of 256-day long time series, with a 206-day overlap between two consecutive segments, were prepared from the entire 4843-day (1997-2008) long time series. Using the fast Fourier transform, time series of daily precipitation anomalies (either symmetric or antisymmetric with respect to the equator) in each segment and latitude are transformed into the wavenumber-frequency domain. Figures. 10 and 11 compare the power spectra of precipitation from the RAs and GPCP for the symmetric and antisymmetric components, respectively.

All power spectra from GPCP and RAs precipitation are red in both space and time, with maximum power in lower wavenumber and frequency. In a number of areas in Figs. 10 and 11, the spectral power exceeds the background spectrum. These signals follow, in the symmetric spectra, the dispersion curves of the Kelvin wave, the n=1 Equatorial Rossby (ER) wave, and the MJO, and in the antisymmetric spectra, the mixed Rossby-gravity (MRG) wave, the n=0 eastward propagating inertia-gravity (EIG) wave, and the MJO. In the following, we focus on how well the RAs represent the amplitude of the spectrum, especially the large-scale convectively coupled wave signals in it.

As shown in Figs. 10 and 11, the two older NCEP RAs show quite different features in the strength of precipitation variability; NCEP/NCAR exhibits variability that is too weak, while it is too strong in NCEP-DOE. This is further illustrated in Figure 12, which shows the spectral power of the waves identified in Figs. 10 and 11 divided by that of GPCP. In Figure 12, the sum of spectral powers over the wavenumber-frequency space for each wave is presented. We use same wavenumber-frequency spaces for the waves that were used in Wheeler and Kiladis (1999), except for the MJO where 30-80 day band instead of 30-96 day is used. It shows that NCEP/NCAR underestimates the variability of all waves. NCEP-DOE shows reasonable variability of the symmetric MJO and the Kelvin wave (close to the magnitude of GPCP), but it exhibits excessive variability in the n=1 ER wave, the antisymmetric MJO and the MRG wave. Also, in both RAs the MJO signal is not as clearly distinguished from the red spectra as in GPCP (Figs. 10 and 11). Compared with the two early RAs, the overall variance pattern in the modern RAs is closer to that of GPCP (Fig. 12), and the MJO signal is more clearly distinguished from the background spectra (Figs. 10 and 11). In Figure 12, the amplitudes of precipitation variance in all waves in ERA-I and MERRA are comparable to each other. These two RAs show somewhat smaller magnitudes than that of GPCP, but much better than NCEP/NCAR. On the other hand, CFSR shows similar wave amplitudes with those from NCEP-DOE in general. The only exception is the n=1 ER wave where the CFSR signal is about half of that in NCEP-DOE so that it is much closer to observed value.

To obtain a metric of the MJO, the sum of power over the MJO band (wavenumber 1-5, period 30-60 days) is divided by that of the westward propagating counterpart. This East/West power ratio metric has been used in previous studies, mostly for evaluating climate models (Kim et al. 2009; Kim et al. 2011; Sperber and Kim 2012). Figure 13 shows the scatter plot of the East/West power ratios from the symmetric and antisymmetric spectra. In the observations, the eastward propagation is more dominant than the westward for MJO. The observed ratios are 1.86 for the symmetric component and 1.23 for the antisymmetric component. All RAs tend to underestimate these ratios, which suggest that the westward propagating components are too strong in their precipitation products. Encouragingly, the modern RAs exhibit higher ratios than the older RAs, especially for the ratio of the symmetric MJO. For the symmetric MJO, the East/West power ratios of NCEP/NCAR and NCEP-DOE are smaller than 1.3, while it is close to (CFSR) or greater than 1.5 (ERA-I and MERRA) in the modern RAs. These are much closer to the observed values.

The coherence squared (Coh^2) and the phase between the RA and GPCP were calculated using a cross-spectrum analysis, presented in Figs. 14 and 15 for the symmetric and the antisymmetric parts, respectively. The cross-spectra are first calculated for each segment and then averaged over all segments. The Coh^2 and the phase of the RA precipitation with GPCP measure how closely precipitation anomalies of RAs follow that of GPCP in time. Ideally, if a RA perfectly reproduces GPCP, the Coh^2 and phase will be one and zero, respectively, for all wave components. Uncertainty exists in GPCP dataset (e.g., Huffman et al. 2007), however, so that we should not expect RAs to perfectly reproduce GPCP. To consider such uncertainties in observations, and to suggest an upper limit for RAs to achieve, the Coh^2 and phase are also computed between two observational dataset - GPCP and TRMM.

In Figs. 14 and 15, the Coh^2 between the RA precipitation and GPCP is actually much smaller than that between TRMM and GPCP for most wavenumber-frequency components (especially for the older RAs). The overall Coh^2 (shaded in Figs. 14 and 15) in the modern RAs is in fact considerably greater than that for the older RAs, with the improvement occurring at all waves (Fig. 16a). In NCEP/NCAR and NCEP-DOE, areas of Coh^2 greater than 0.5 are mostly limited to within the MJO wave band, whereas CFSR, ERA-I, and MERRA show much broader areas with values more than 0.5. By comparison, TRMM exhibits Coh^2 greater than 0.5 in most areas. In particular, the Coh^2 of the symmetric MJO is greater than 0.6 in ERA-I and MERRA. For the Kelvin wave and the MRG wave, these two RAs exhibit much greater coherence with the observations compared to the NCEP RAs.

In many regions of the space-time spectra (Figs. 14 and 15), the phase is near zero in the modern RAs. For all five RAs, the absolute value of the phase difference for the symmetric MJO, the n=1 ER wave, and the phase difference for the antisymmetric MJO is smaller than 10 degree (Fig. 16b), except for the symmetric MJO of ERA-I. The modern RAs, however, show non-negligible phase differences from GPCP for the high-frequency waves, such as Kelvin and MRG waves. Figure 16b shows that the Kelvin wave components in the modern RAs systematically lag GPCP by 10-20 degrees, while the MRG components lead GPCP by about 20 degrees. This systematic difference cannot be attributed to the observational uncertainty as TRMM shows nearly zero phase difference for these waves.

4. Summary and Conclusion

This study assessed the quality of the time-mean and subseasonal variability of the tropical precipitation produced by five global RAs. Twelve-year-long (1997-2008) precipitation data from three generations of RA products from NCEP (NCEP/NCAR, NCEP-DOE, and CFSR), and the recent RA products from ECMWF (ERA-I) and NASA (MERRA) were compared with GPCP observations. Eleven-year-long (1998-2008) TRMM precipitation data is also used in the evaluation, namely to assess observational uncertainties. The analysis includes an examination of the boreal winter and summer means, probability distribution of rain intensity, and subseasonal (20-100 day) variability, as well as wavenumber-frequency power spectra and cross-spectra with observed precipitation.

The three modern RAs (CFSR, ERA-I, and MERRA) exhibit an overall improved representation of the seasonal mean state when compared to the older RAs (NCEP/NCAR and NCEP-DOE). Over the Indian Ocean, where many MJO events are initiated, the modern RAs are able to capture the zonal gradient of precipitation (which increases to the east), while the older RAs exhibit peaks in the west or the center of the basin. The modern RAs show a weaker (improved) double ITCZ bias in the eastern Pacific. The contrast in magnitude between the time-mean precipitation and the subseasonal variance over land is well-captured in all RAs. Despite of the improvement in the pattern of seasonal mean precipitation, the probability distribution of daily rain rates in the modern RAs exhibits no systematic difference from that in the old RAs. The amplitude of subseasonal variability over the tropics is closer to the observed in the modern RAs while it is either too weak (NCEP/NCAR) or too strong (NCEP-DOE) in the older RAs. It is also found that the magnitudes of mean and the subseasonal variance of precipitation anomalies in the tropics show a monotonic proportional relationship across RAs. But RAs also exhibit a systematic wet bias in their mean tropical rainfall.

A wave number frequency analysis shows that both observations and RAs contain a number of identifiable wave structures including: the symmetric and antisymmetric MJO, the Kelvin wave, the n=1 ER wave, and the MRG wave. NCEP/NCAR underestimates the power of all waves considered here. NCEP-DOE reproduces the amplitude of the symmetric MJO and the Kelvin wave reasonably well, although it shows excessive power for the n=1 ER wave, the antisymmetric MJO, and the MRG wave. CFSR is similar to NCEP-DOE in representing the amplitude of the waves, although the too-strong bias for the n=1 ER wave in NCEP-DOE is significantly improved. ERA-I and MERRA underestimate the amplitude of all waves, but are an overall improvement over NCEP/NCAR. TRMM shows the coherence with GPCP greater than those of RAs for all waves, suggesting the bias in the coherence cannot be solely attributed to the observational uncertainties. Nonetheless, the modern RAs have greater coherence with GPCP than the older RAs. Especially, the coherence squared between GPCP and precipitation from modern RAs in MJO band is much higher than that of old RAs. Despite of the notable improvement in the coherence for the MJO, the coherence for other CCEWs are still limited. Also, all RAs including the modern ones have a systematic phase bias for the high-frequency waves (the Kelvin and MRG waves). These limitations call for further improvement of the RAs, possibly through additional observational resources related to precipitation and through more holistic, multi-variate data assimilation methodology.

This study leaves a detailed analysis of impacts driven by assimilating moisture-related satellite radiances in the modern RAs for further study, which are speculated as at least one of the potential sources for the improvement from the old RAs in the representation of MJO and CCEWs. Because all components in the assimilation system (e.g., assimilated observations, assimilation technique, and forecast model) have their own influences on the quality of a resulted RA, it is not easy to disentangle specific contributions made by the moisture assimilation, and this is well beyond the scope of this study. A set of systematic data-denial experiments in a data assimilation mode will help us to identify the importance of the moisture assimilation in the quality of RAs in representing mean-state and subseasonal variability of precipitation.

Acknowledgements

This work was supported by the Korea Meteorological Administration Research and

Development Program under Grant APCC 2013-3141. Also, this work was supported by the NASA Modeling, Analysis, and Prediction (MAP) program for SDS. DEW's and BT's contribution to this research was performed at Jet Propulsion Laboratory (JPL), California Institute of Technology (Caltech), under a contract with National Aeronautics and Space Administration (NASA). The authors are grateful for the computing resources provided by NASA and the Supercomputing Center at Korea Institute of Science and Technology Information (KSC-2013-C2-011).

References

Bechtold, P., E. Bazile, F. Guichard, P. Mascart, and E. Richard, 2001: A mass-flux convection scheme for regional and global models. Q.J.R. Meteorol. Soc., 127: 869–886. doi: 10.1002/qj.49712757309.

Behrangi, A., M. Lebsock, S. Wong, and B. Lambrigtsen, 2012: On the quantification of oceanic rainfall using spaceborne sensors. J. Geophys. Res., **117**, D20105.

Bergman, J. W., H. H. Hendon, and K. M. Weickmann, 2001: Intraseasonal air-sea interactions at the onset of El Nin˜o, J. Clim., 14, 1702– 1719.

Bessafi, M., and M. C. Wheeler, 2006: Modulation of South Indian Ocean tropical cyclones by the Madden–Julian oscillation and convectively coupled equatorial waves. Mon. Wea. Rev., 134, 638–656.

Bloom, S. C., L. L. Takacs, A. M. da Silva, and D. Ledvina, 1996: Data Assimilation Using Incremental Analysis Updates. Mon. Wea. Rev., 124, 1256–1271.

Compo, G.P., and Coauthors, 2011: The Twentieth Century Reanalysis Project. Q. J. Roy. Meteorol. Soc. 137, 1-28.

Dee, D.P., and Coauthors, 2011: The ERA-Interim reanalysis: Configuration and performance of the data assimilation system. Q. J. Roy. Meteorol. Soc., 137, 553-597.

Derber, J. C., D. F. Parrish, and S. J. Lord, 1991: The New Global Operational Analysis System at the National Meteorological Center. Wea. Forecasting, 6, 538-547.

Frank, W. M., and P. E. Roundy, 2006: The role of tropical waves in tropical cyclogenesis. Mon. Wea. Rev., 134, 2397–2417.

Frierson, D. M. W., D. Kim, I.-S. Kang, M.-I. Lee, J.L. Lin, 2011: Structure of AGCM-Simulated Convectively Coupled Kelvin Waves and Sensitivity to Convective Parameterization. *J. Atmos. Sci.*, **68**, 26–45.

Hendon H. H. and Wheeler M. C., 2008: Some Space–Time Spectral Analyses of Tropical Convection and Planetary-Scale Waves. J. Atmos. Sci., 65, 2936-2948

Hodges, K. I., R. W. Lee, and L. Bengtsson, 2011: A Comparison of Extratropical Cyclones in Recent Reanalyses ERA-Interim, NASA MERRA, NCEP CFSR, and JRA-25. J. Climate, 24, 4888–4906.

Hong, S.-Y., and H.-L. Pan, 1998: Convective Trigger Function for a Mass-Flux Cumulus Parameterization Scheme. Mon. Wea. Rev., 126, 2599–2620.

Huffman, G. J.,, R. F. Adler, M. Morrissey, D. T. Bolvin, S. Curtis, R. Joyce, B. McGavock, and J. Susskind, 2001: Global precipitation at one-degree daily resolution from multisatellite observations. J. Hydrometeor., 2, 36–50.

Huffman, G. J., and Coauthors, 2007: The TRMM Multisatellite Precipitation Analysis (TMPA): Quasi-Global, Multiyear, Combined-Sensor Precipitation Estimates at Fine Scales. J. Hydrometeor, 8, 38–55. doi: http://dx.doi.org/10.1175/JHM560.1

Hung, M.-P., J.-L. Lin, W. Wang, D. Kim, T. Shinoda, and S. J. Weaver, 2013: MJO and Convectively Coupled Equatorial Waves Simulated by CMIP5 Climate Models. J. Climate, revised.

Kalnay, E., and coauthors, 1996: The NCEP/NCAR 40-Year Reanalysis Project. Bull. Amer. Meteor. Soc., 77, 437-471.

Kanamitsu, M., W. Ebisuzaki, J. Woolen, S.-K. Yang, J. J. Hnilo, M. Fiorino, and G. L. Potter, 2002: NCEP-DOE AMIP-II Reanalysis (R-2). Bull. Amer. Meteor. Soc., 83, 1631-1643.

Kessler, W. S., and R. Kleeman, 2000: Rectification of the Madden-Julian Oscillation into the ENSO cycle, J. Clim., 13, 3560– 3575.

Kiladis, G. N.,, M. C. Wheeler, P. T. Haertel, K. H. Straub, and P. E. Roundy, 2009: Convectively coupled equatorial waves. Rev. Geophys., 47, RG2003, doi:10.1029/2008RG000266.

Kim, D., and Coauthors, 2009: Application of MJO Simulation Diagnostics to Climate Models. J. Climate, 22, 6413–6436. doi: http://dx.doi.org/10.1175/2009JCLI3063.1

Kim, D., A. H. Sobel, E. D. Maloney, D. M. W. Frierson, and I.-S. Kang, 2011: A Systematic Relationship between Intraseasonal Variability and Mean State Bias in AGCM Simulations., J. Climate, 24, 5506–5520. doi: http://dx.doi.org/10.1175/2011JCLI4177.1

Kleist, D.T., D.F. Parrish, J.C. Derber, R. Treadon, W.-S. Wu and S. Lord, 2009: Introduction of the GSI into the NCEP Global Data Assimilation System. Wea. Forecasting, 24, 1691–1705.

Liebmann, B., H. H. Hendon, and J. D. Glick, 1994: The relationship between tropical cyclones of the western Pacific and Indian Oceans and the Madden–Julian oscillation. J. Meteor. Soc. Japan, 72, 401–412.

Lin, J.-L., and Coauthors, 2006: Tropical Intraseasonal Variability in 14 IPCC AR4 Climate Models. Part I: Convective Signals. J. Climate, 19, 2665–2690.

Majda, A., and S. Stechmann (2011), Multi-scale theories for the MJO, in *Intraseasonal Variability of the Atmosphere-Ocean Climate System, 2nd Edition*, edited by W. K. M. Lau and D. E. Waliser, p. 613, Springer, Heidelberg, Germany.

Madden R. A. and Julian P. R., 1972: Description of global-scale circulation cells in the tropics with a 40‑50 day period., J. Atmos. Sci., 29, 1109‑1123

Maloney, E. D., and D. L. Hartmann, 2000a: Modulation of hurricane activity in the Gulf of Mexico by the Madden–Julian oscillation. Science, 287, 2002–2004.

Maloney, E. D., and D. L. Hartmann, 2000b: Modulation of eastern North Pacific hurricanes by the Madden–Julian oscillation. J. Climate, 13, 1451–1460.:

Matsuno, T., 1966: Quasi-geostrophic motions in the equatorial area, J. Meteorol. Soc. Jpn., 44, 25‑43.

Matthews, A.J., 2008: Primary and successive events in the Madden–Julian Oscillation. *Quart. J. Roy. Meteorol. Soc.*, **134**:631, 439-453.

Molinari, J., K. Lombardo, and D. Vollaro, 2007: Tropical cyclogenesis within an equatorial Rossby wave packet. J. Atmos. Sci., 64, 1301–1317.

Moorthi, S., and M.J. Suarez, 1992: Relaxed Arakawa-Schubert. A parameterization of moist convection for general circulation models. Mon. Wea. Rev., 120, 978–1002.

Onogi, K., and co-authors, 2007: The JRA-25 Reanalysis. J. Meteor. Soc. Japan, 85, 369-432. doi: 10.2151/jmsj.85.369.

Pan, H.-L., and W.-S. Wu, 1994: Implementing a mass-flux convective parameterization package for the NMC Medium Range Forecast Model. Preprints, 10th Conf. on Numerical Weather Prediction, Portland, OR, Amer. Meteor. Soc., 96-98.

Parrish, D. F., and J. C. Derber, 1992: The National Meteorological Center's Spectral Statistical Interpolation Analysis System. Mon. Wea. Rev., 120, 1747-1763.

Rančić, M., J. C. Derber, D. Parrish, R. Treadon, and D. T. Kleist, 2008: The development of the first-order time extrapolation to the observation (FOTO) method and its application in the NCEP global data assimilation system. Proc. 12th Conf. IOAS-AOLS, New Orleans, LA, Amer. Meteor. Soc., 6.1. http://ams.confex.com/ams/88Annual/ techprogram/paper_131816.htm.

Rienecker, M.M., and coauthors, 2011. MERRA - NASA's Modern-Era Retrospective Analysis for Research and Applications. J. Climate, 24, 3624-3648, doi: 10.1175/JCLI-D-11-00015.1.

Saha, S. and coauthors, 2010: The NCEP Climate Forecast System Reanalysis. Bull. Amer. Meteor. Soc., 91, 8, 1015-1057.

Sobel, A. H., et al., 2008: The role of surface heat fluxes in tropical intraseasonal oscillations, Nat. Geosci., 1, 653–657, doi:10.1038/ngeo312.

Sperber, K. R., 2003: Propagation and the Vertical Structure of the Madden–Julian Oscillation. *Mon. Wea. Rev.*, **131**, 3018–3037.

Sperber, K., J. Slingo, and P. Inness (2011), Modeling Intraseasonal Variability, in *Intraseasonal Variability of the Atmosphere-Ocean Climate System, 2nd Edition*, edited by W. K. M. Lau and D. E. Waliser, p. 613, Springer, Heidelberg, Germany.

Sperber, K.R., and D. Kim, 2012: Simplified metrics for the identification of the Madden-Julian Oscillation in models. Atmos. Sci. Lett., in press.

Takayabu YN, Iguchi T, Kachi M, Shibata A, Kanzawa H, 1999: Abrupt termination of the 1997–1998 El Nino in response to a Madden-Julian oscillation, Nature, 402, 279–282

Taylor, K. E., 2001: Summarizing multiple aspects of model performance in a single diagram. *J. Geophys. Res*, **106(D7)**, 7183-7192.

Tian, B.J., D. E. Waliser, and E. Fetzer, 2006: Modulation of the Diurnal Cycle of Deep Convective Clouds by the Madden-Julian Oscillation. Geophys. Res. Lett., 30, L20704, 10.1029/2006GL027752.

Uppala, S., and coauthors, 2005: The ERA-40 Re-Analysis. Quart. J. Roy. Meteor. Soc., 131, 2961-3012.

Wheeler, M. C. and J. L. McBride, 2005: Intraseasonal Variability in the Atmosphere-Ocean Climate System, W. K.-M. Lau and D. E., Waliser, Eds., Praxis Publishing, 125-173.

Wheeler, M. C. and G.N. Kiladis, 1999: Convectively coupled Equatorial Waves: Analysis of clouds and temperature in the wavenumber–frequency domain. J. Atmos. Sci., 56, 374-399.

Wang, B., 2005: Theory. Intraseasonal Variability in the Atmosphere, Ocean Climate System, W. K.-M. Lau and D. Waliser, Eds., Springer-Praxis, 307–351.

Wang, B. (2011), Theory, in *Intraseasonal Variability of the Atmosphere-Ocean Climate System, 2nd Edition*, edited by W. K. M. Lau and D. E. Waliser, p. 613, Springer, Heidelberg, Germany.

Yang, G.-Y., B. Hoskins, J. Slingo, 2007: Convectively Coupled Equatorial Waves. Part I: Horizontal and Vertical Structures. *J. Atmos. Sci.*, **64**, 3406–3423.

Yasunari, T., 1979: Cloudiness Fluctuations Associated with the Northern Hemisphere Summer Monsoon. J. Metor. Soc. Japan, 57-3, 227-242.

Zhang, C., 2005: Madden-Julian oscillation. Rev. Geophys., 43, RG2003, doi:10.1029/2004RG000158.

Zhang, M. H and coauthors, 2005: Comparing clouds and their seasonal variations in 10 atmospheric general circulation models with satellite measurements., J. Geophys. Res., 110, D15S02, doi:10.1029/2004JD005021.

Table list

Figure list

Figure 1. November-April mean precipitation of a) NCEP/NCAR, b) NCEP-DOE, c) CFSR, d) ERA-I, e) MERRA, f) GPCP, and g) TRMM. Unit is mm day^{-1}.

Figure 2. Same as Figure 1, except for May-October mean precipitation.

Figure 3. A Taylor diagram of November-April (open circles) and May-October (crosses) mean precipitation over the tropics (0-360°E, 30°S-30°N).

Figure 4. Probability density of precipitation over a) Warm Pool (40-180°E, 20°S-20°N), b) ITCZ (182.5-280°E, 2.5-10°N), and c) South Eastern Pacific (220-280°E, 2.5-10°S) regions.

Figure 5. As in Figure 1, except for variance of 20-100 day band pass filtered precipitation. The unit is mm^2 day^{-2}.

Figure 6. Same as Figure 3, except for May-October variance of 20-100 day band pass filtered precipitation.

Figure 7. As in Figure 3, except for variance of 20-100 day band pass filtered precipitation.

Figure 8. Ratio of 20-100 day variability to total variability (November-April).

Figure 9. November-April (open circles) and May-October (crosses) scatter plot between standard deviation of 20-100 day filtered precipitation anomalies and tropics (0-360°E, 30°S-30°N) mean of precipitation. Units for both quantities are mm day^{-1}.

Figure 10. Symmetric wavenumber-frequency spectra of a) NCEP/NCAR, b) NCEP-

DOE, c) CFSR, d) ERA-I, e) MERRA, and f) GPCP. Dispersion curves for the (n = -1) Kelvin, n = 1 equatorial Rossby (ER) modes, corresponding to three equivalent depths (h = 12, 25, and 50 m) in the shallow water equations are overlaid (red contours). MJO is defined as the spectral components within zonal wavenumbers 1 to 3 and having periods 30 to 80 days. (add significance by dividing power by background power)

Figure 11. Same as Figure 10, except for antisymmetric spectra. Dispersion curves for n = 0 eastward intertio-gravity (EIG), and mixed Rossby–gravity (MRG) modes, corresponding to three equivalent depths (h = 12, 25, and 50 m) in the shallow water equations are overlaid (red contours). MJO is defined as the spectral components within zonal wavenumbers 1 to 3 and having periods 30 to 80 days.

Figure 12. Ratio of powers corresponding to each wave in reanalysis and TRMM to that in GPCP.

Figure 13. Scatter plot between East/West power ratios of symmetric and antisymmetric MJO.

Figure 14. Coherence squared (colors) and phase lag (vectors) between GPCP precipitation and precipitation from a) NCEP/NCAR, b) NCEP-DOE, c) CFSR, d) ERA-I, e) MERRA, and f) TRMM. The symmetric spectrum is shown. Spectra were computed at individual latitude, and then averaged over 15^{o}S–15^{o}N. Computations are conducted using data in all seasons on 256-day segments,

overlapping by 206 days. Vectors represent the phase by which reanalysis precipitation lags GPCP, increasing in the clockwise direction. A phase of 0^{o} is represented by a vector directed upward.

Figure 15. Same as Figure 14, except for antisymmetric spectra.

Figure 16. a) Coherence squared and b) the phase (deg) averaged for the waves from Figure 14 and 15.

Table 1. Description of the reanalyses used in this study.

Reanalysis	Resolution	Convection scheme	Assimilation scheme
NCEP/NCAR (Kalnay et al, 1996)	T62/L28 (top: ~3hPa)	A simplified Arakawa-Schubert convective parameterization (Pan and Wu 1994)	SSI
NCEP-DOE (Kanamitsu et al. 2002)	T62/L28 (top: ~3hPa)	Minor tuning of one in NCEP/NCAR	Same as in NCEP/NCAR
CFSR (Saha et al. 2010)	T382/L64 (top: 0.2hPa)	Addition of Hong and Pan (1998) modification and momentum mixing to one in NCEP/NCAR	GSI, FOTO
ERA-I (Dee et al. 2011)	T255/L60 (top: 0.1 hPa)	A modified version of Bechtold et al. (2001)	GSI, IAU
MERRA (Rienecker et al. 2011)	0.67^{o}x0.5^{o}/L72 (top: 0.01 hPa)	A modified version of the relaxed Arakawa-Schubert convective scheme (Moorthi and Suarez 1992)	4DVAR

4DVAR: Four-dimensional variational assimilation
FOTO: First-order time interpolation to the observation (Rancić et al. 2008)
GSI: Gridded statistical interpolation (Kleist et al. 2009)
IAU: Incremental Analysis Update (Bloom et al. 1996)
SSI: Spectral Statistical Interpolation (Parrish and Derber, 1992, Derber et al., 1991)

Table 2. Summary of satellite radiance data used to constrain tropospheric humidity.

Satellites	Instruments	Reanalyses
NOAA-10, 11, 12, 14	HIRS	CFSR, ERA-I, MERRA
NOAA-15, 16, 17, 18, 19	AMSU-A, AMSU-B (16, 17), HIRS, MHS (18, 19)	CFSR, ERA-I, MERRA
METOP-A	AMSU-A, MHS, HIRS	CFSR, ERA-I
EOS-Aqua	AIRS, AMSR-E, AMSU-A	CFSR, ERA-I, MERRA
DMSP F-8, 10, 11, 13, 14, 15, 16	SSM/I (up to 15), SSMIS (16)	ERA-I, MERRA (except for 16)
GEOS-8, 9, 10, 11, 12, 13	Infrared imager	CFSR, ERA-I, MERRA
METEOSAT-5, 7, 8, 9	Infrared imager	ERA-I
MTSAT-1R	Infrared imager	ERA-I

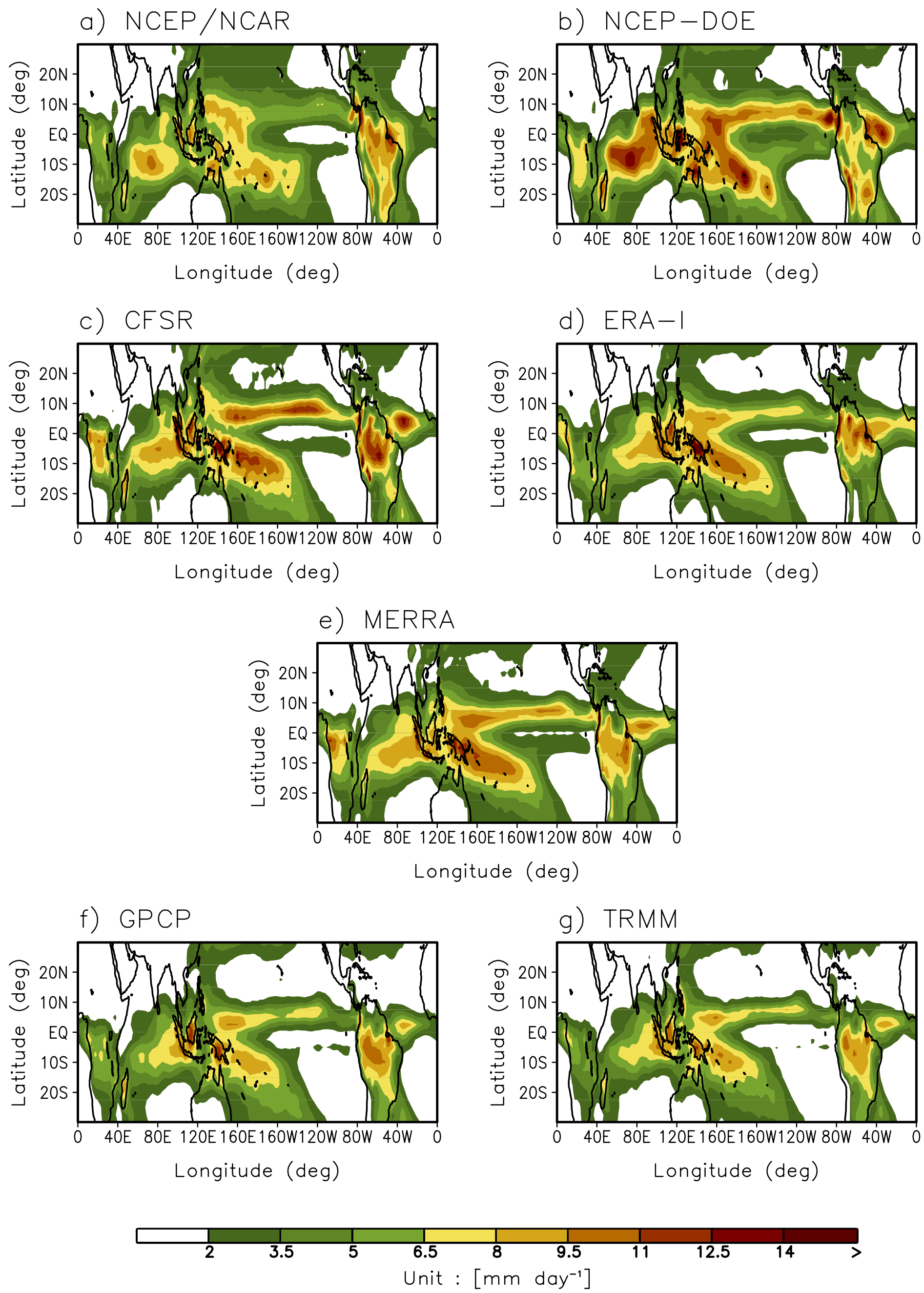

Figure 1. November-April mean precipitation of a) NCEP/NCAR, b) NCEP-DOE, c) CFSR, d) ERA-I, e) MERRA, f) GPCP, and g) TRMM. Unit is mm day^{-1}.

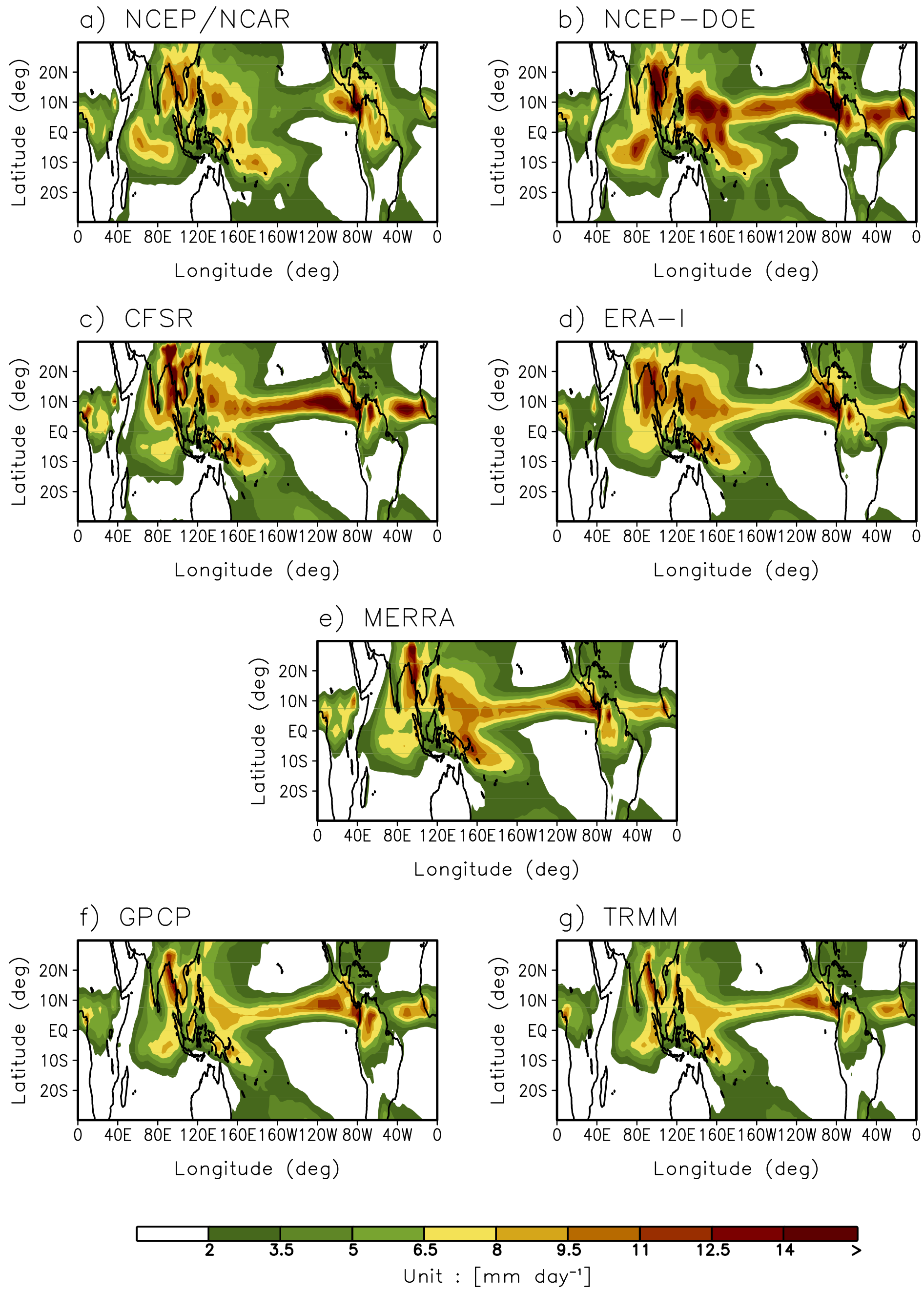

Figure 2. Same as Figure 1, except for May-October mean precipitation.

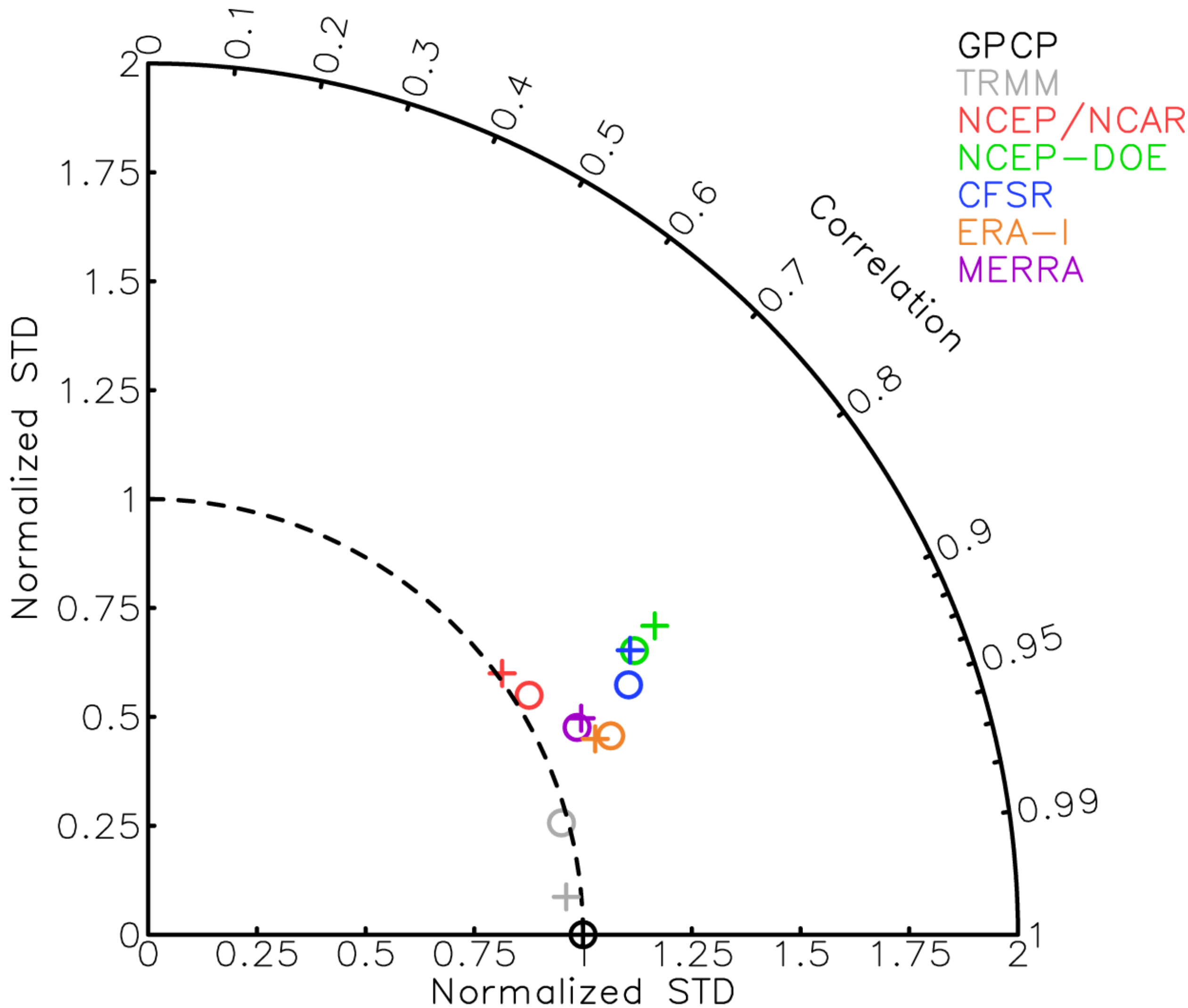

Figure 3. A Taylor diagram of November-April (open circles) and May-October (crosses) mean precipitation over the tropics (0-360°E, 30°S-30°N).

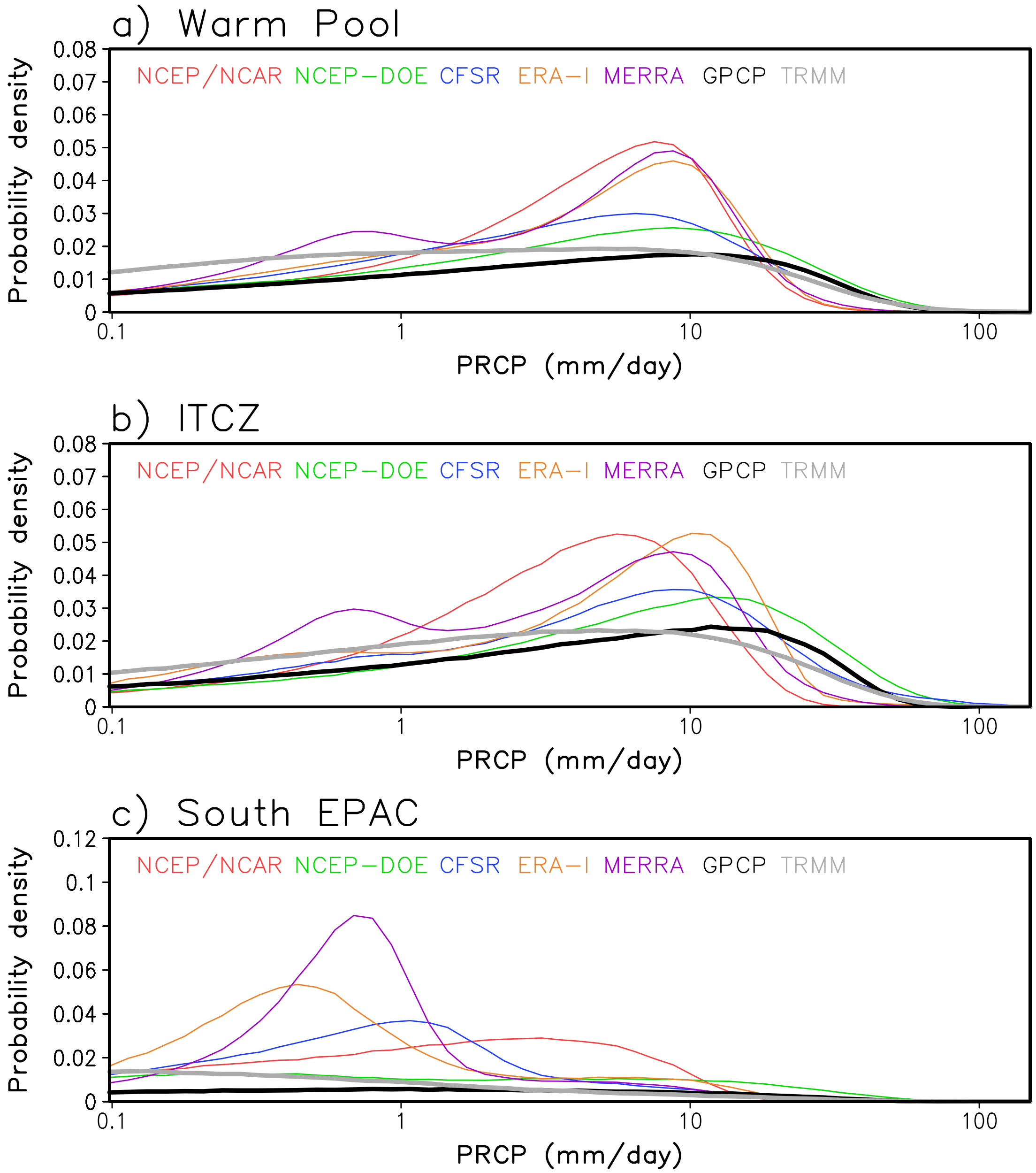

Figure 4. Probability density of precipitation over a) Warm Pool (40-180°E, 20°S-20°N), b) ITCZ (182.5-280°E, 2.5-10°N), and c) South Eastern Pacific (220-280°E, 2.5-10°S) regions.

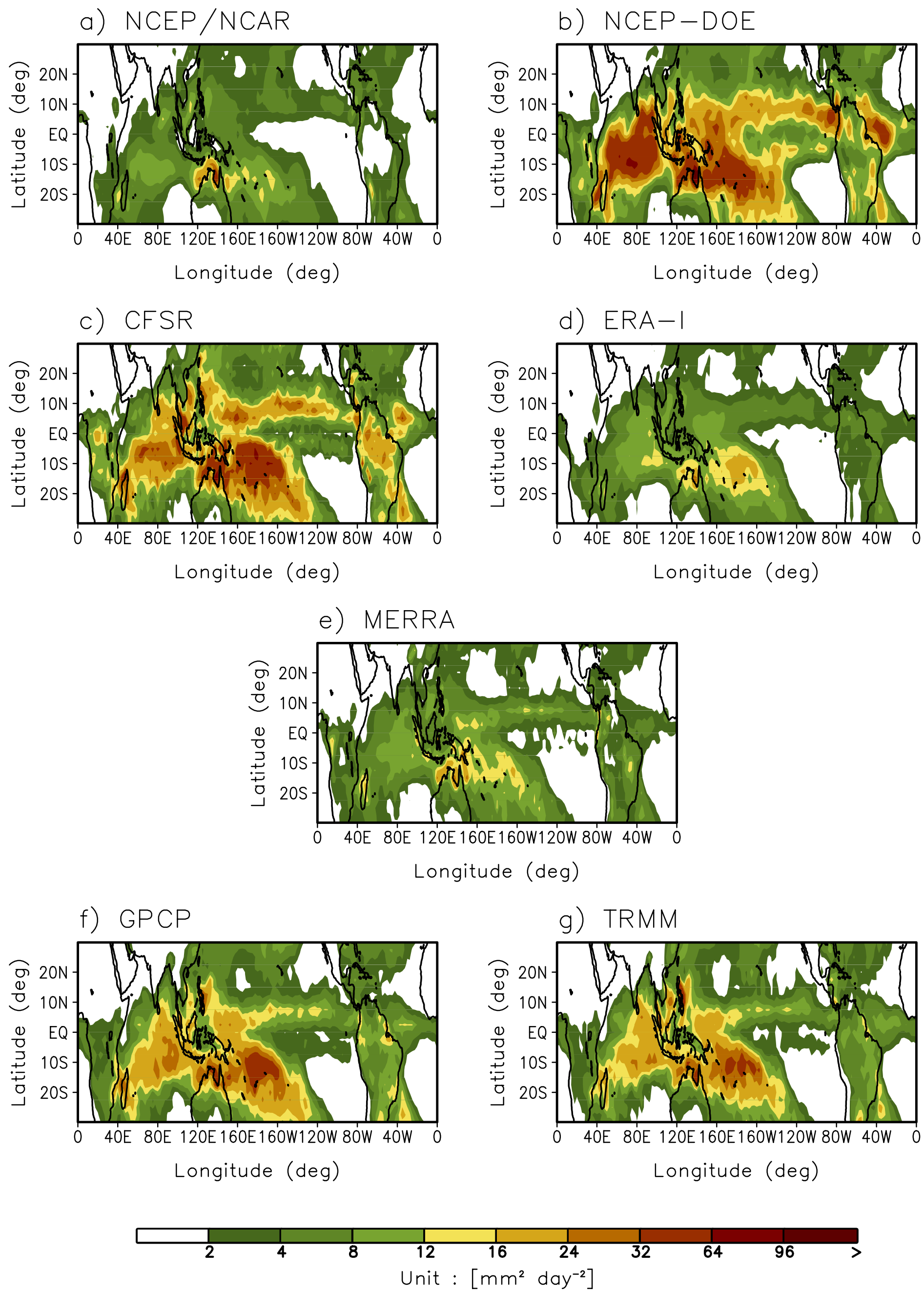

Figure 5. As in Figure 1, except for variance of 20-100 day band pass filtered precipitation. The unit is $mm^2\ day^{-2}$.

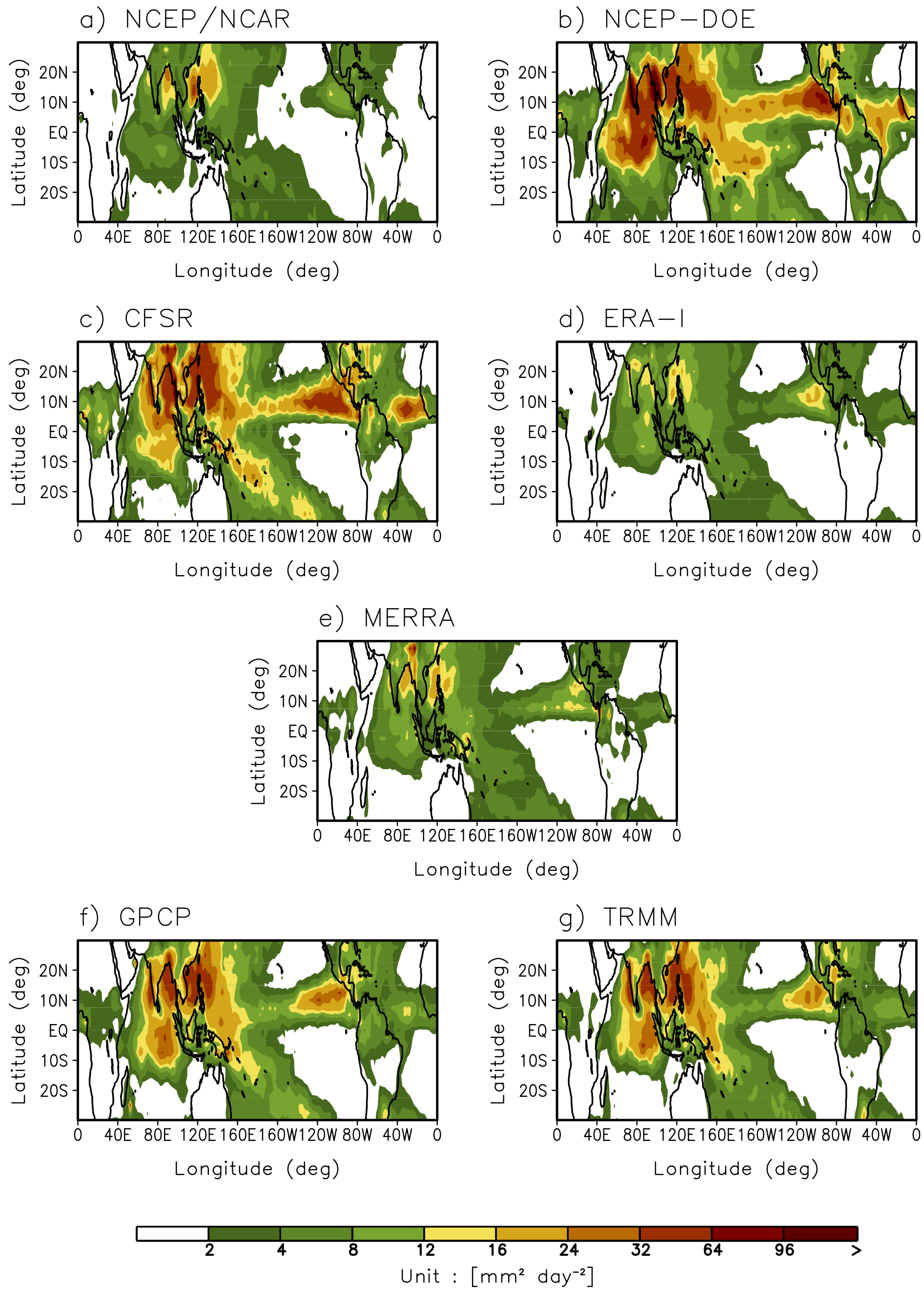

Figure 6. Same as Figure 3, except for May-October variance of 20-100 day band pass filtered precipitation.

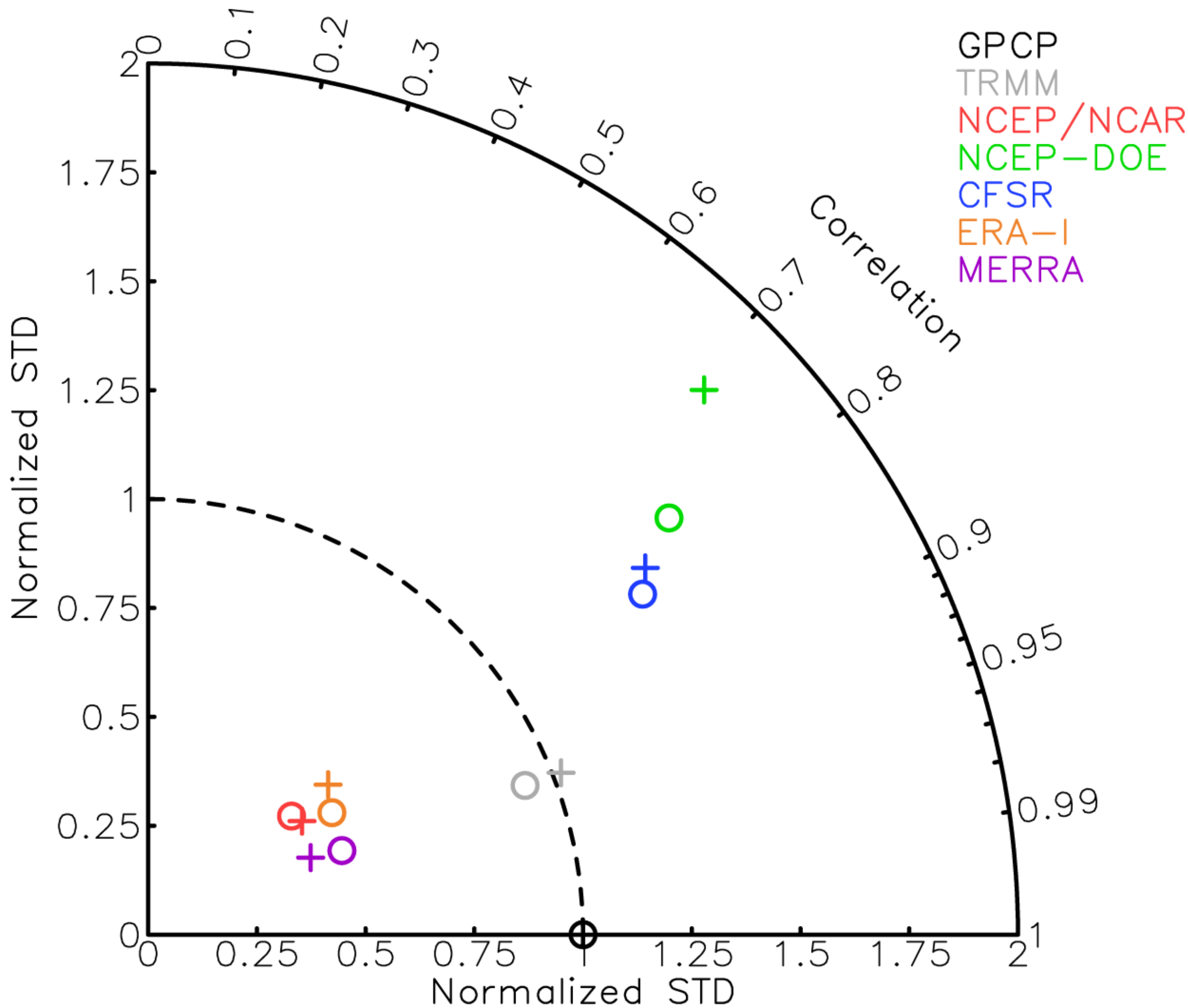

Figure 7. As in Figure 3, except for variance of 20-100 day band pass filtered precipitation.

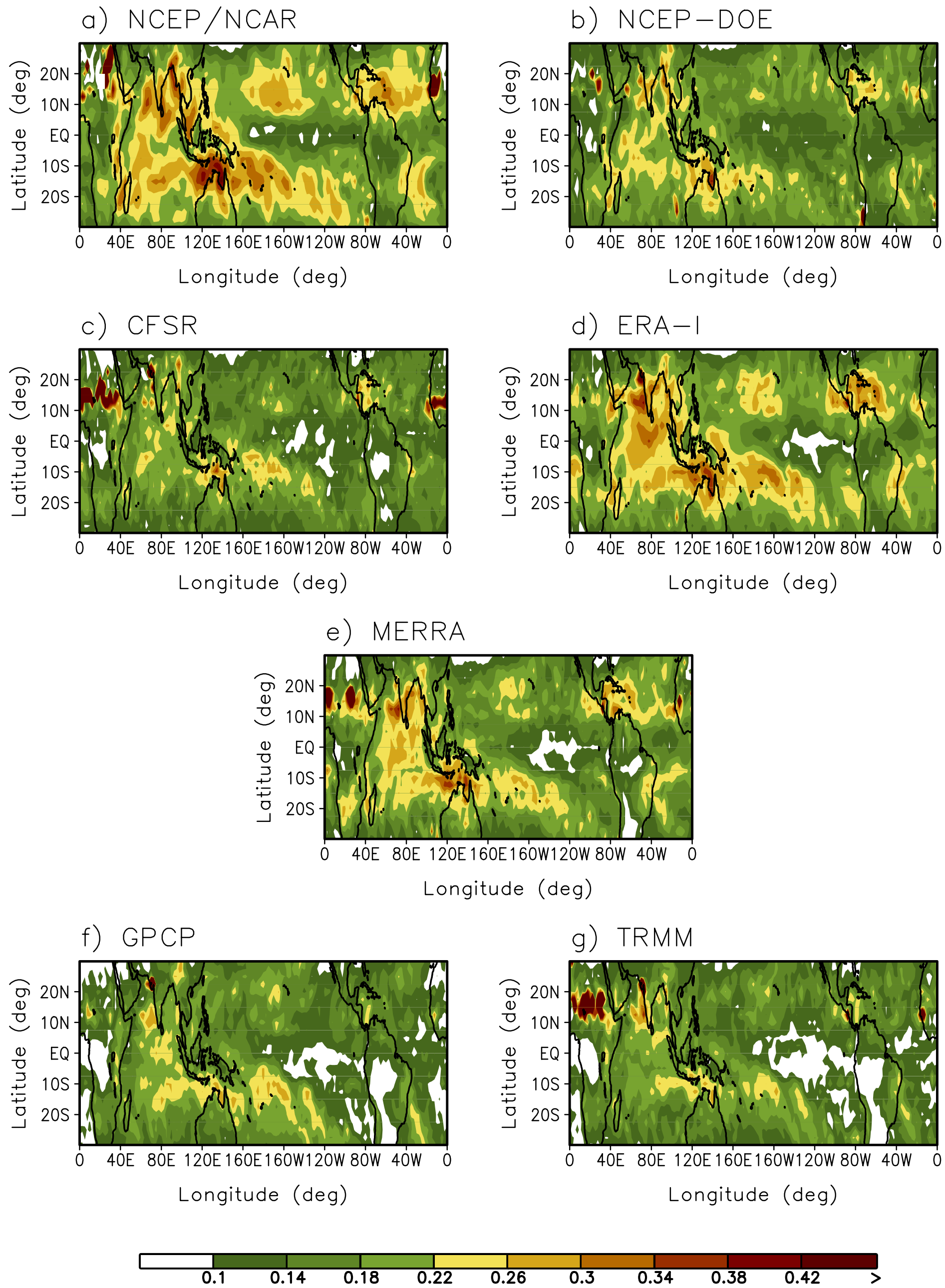

Figure 8. Ratio of 20-100 day variability to total variability (November-April).

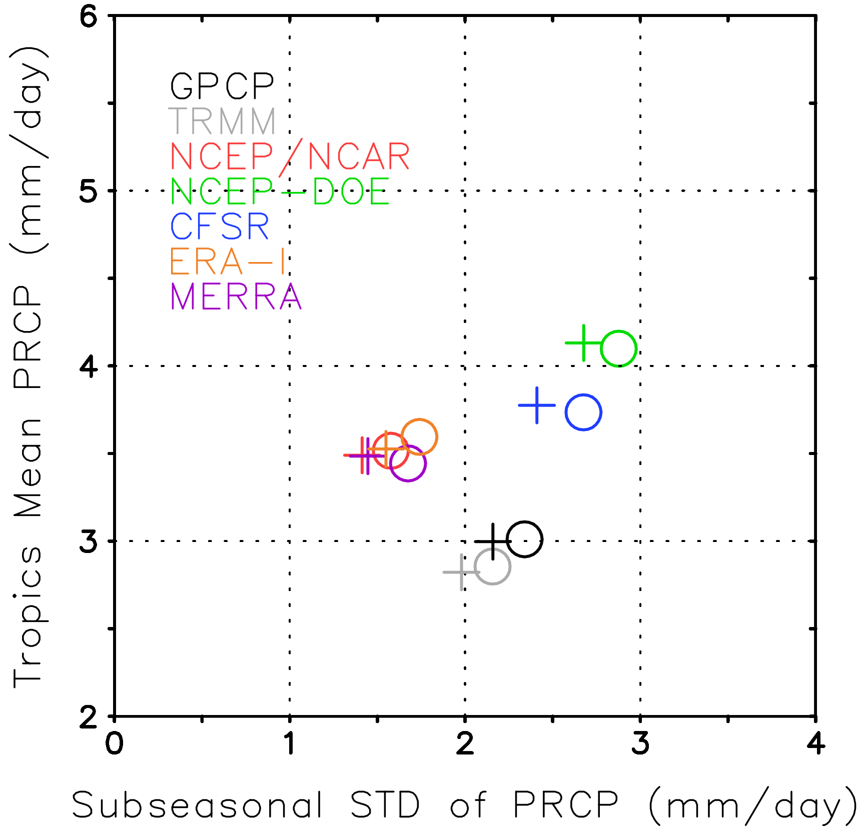

Figure 9. November-April (open circles) and May-October (crosses) scatter plot between standard deviation of 20-100 day filtered precipitation anomalies and tropics (0-360°E, 30°S-30°N) mean of precipitation. Units for both quantities are mm day^{-1}.

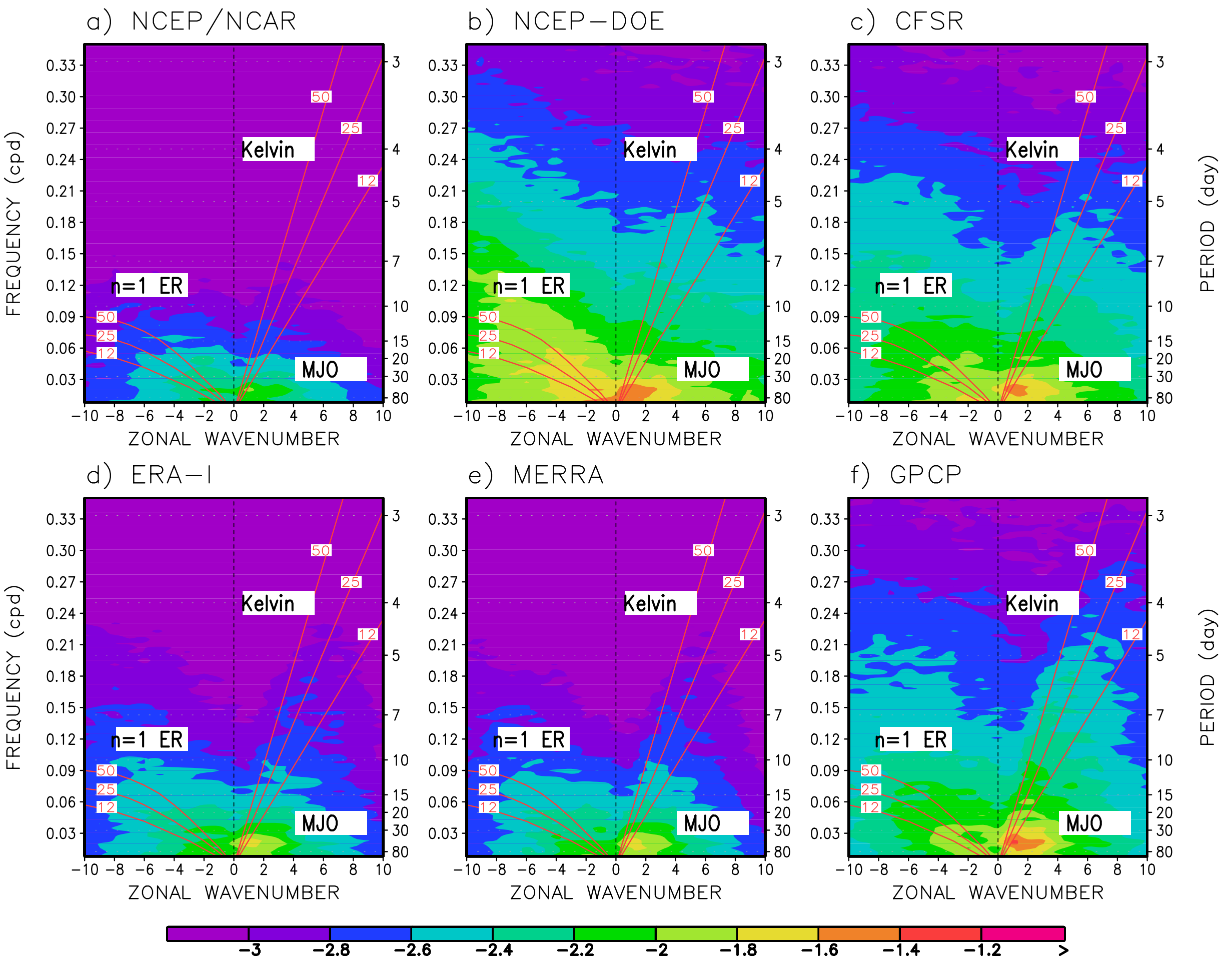

Figure 10. Symmetric wavenumber-frequency spectra of a) NCEP/NCAR, b) NCEP-DOE, c) CFSR, d) ERA-I, e) MERRA, and f) GPCP. Dispersion curves for the (n = -1) Kelvin, n = 1 equatorial Rossby (ER) modes, corresponding to three equivalent depths (h = 12, 25, and 50 m) in the shallow water equations are overlaid (red contours). MJO is defined as the spectral components within zonal wavenumbers 1 to 3 and having periods 30 to 80 days. (add significance by dividing power by background power)

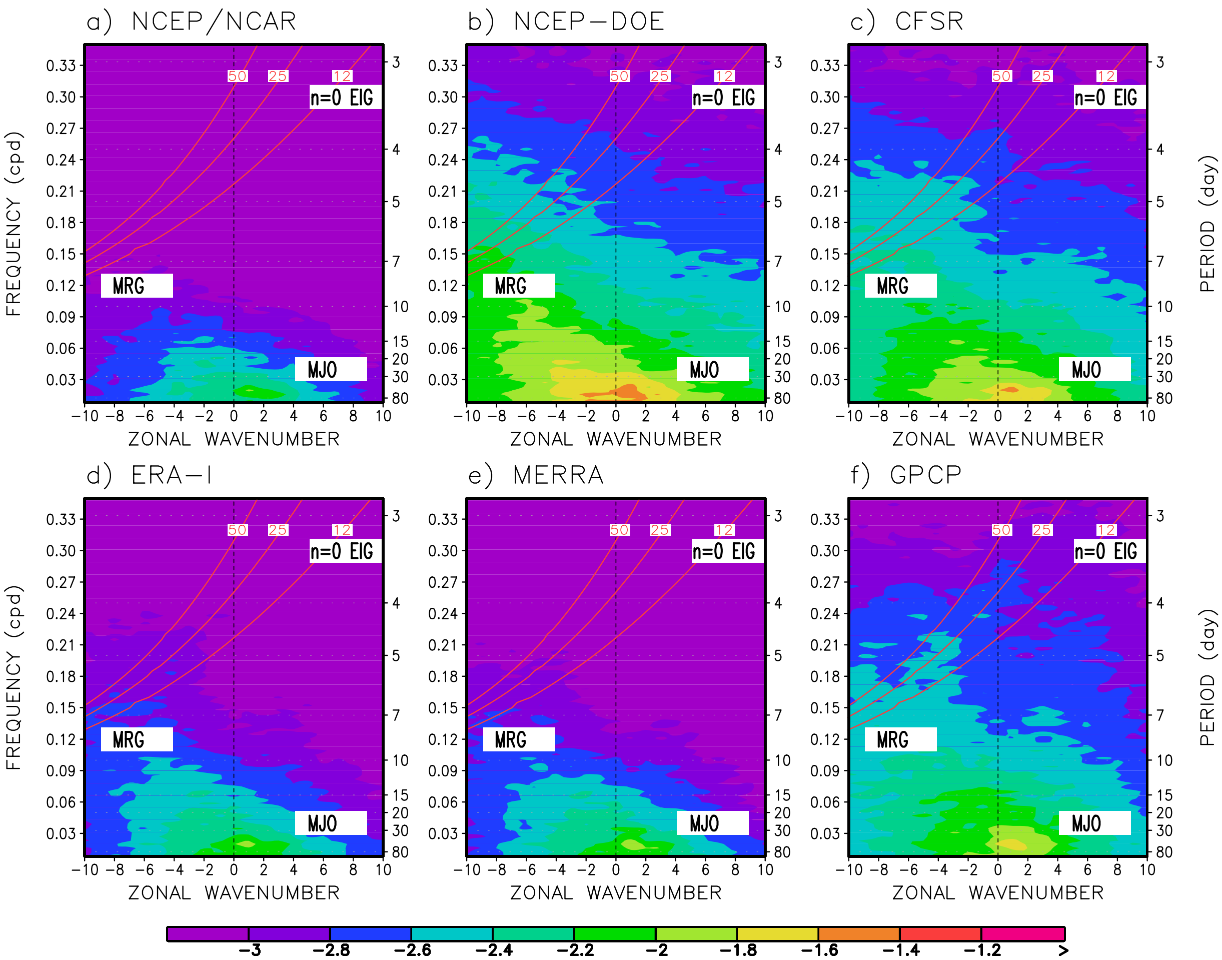

Figure 11. Same as Figure 10, except for antisymmetric spectra. Dispersion curves for n = 0 eastward intertio-gravity (EIG), and mixed Rossby–gravity (MRG) modes, corresponding to three equivalent depths (h = 12, 25, and 50 m) in the shallow water equations are overlaid (red contours). MJO is defined as the spectral components within zonal wavenumbers 1 to 3 and having periods 30 to 80 days.

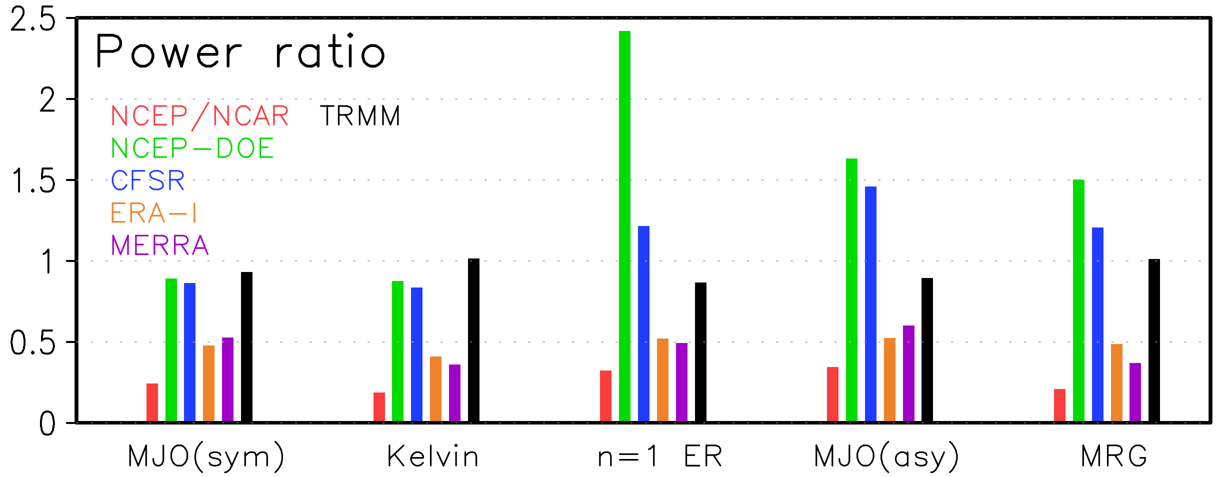

Figure 12. Ratio of powers corresponding to each wave in reanalysis and TRMM to that in GPCP.

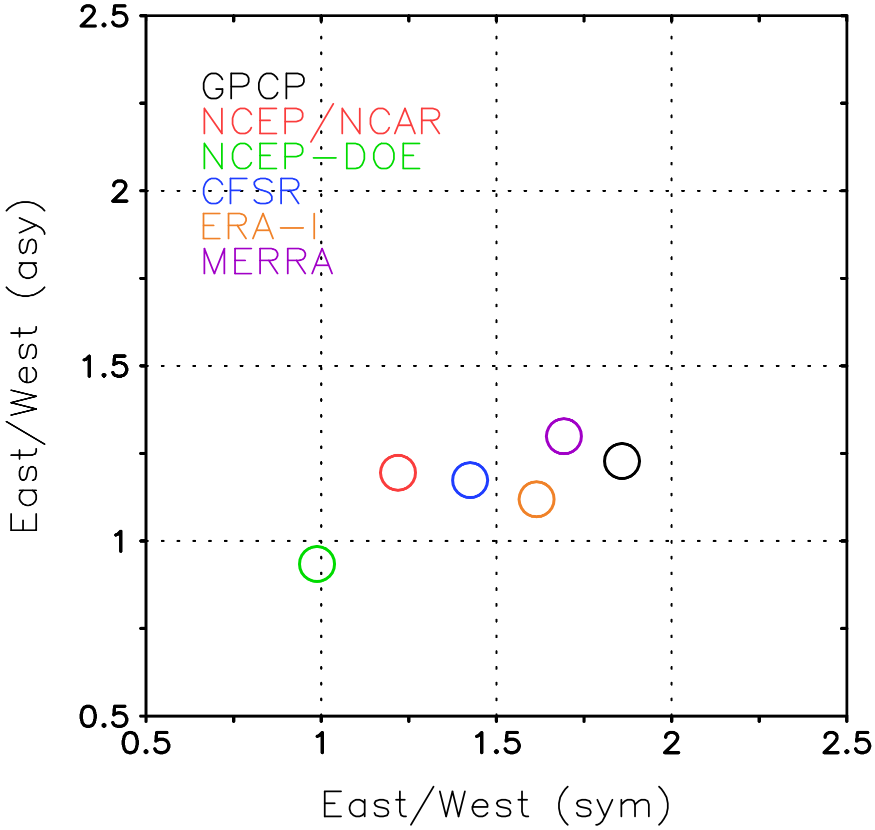

Figure 13. Scatter plot between East/West power ratios of symmetric and antisymmetric MJO.

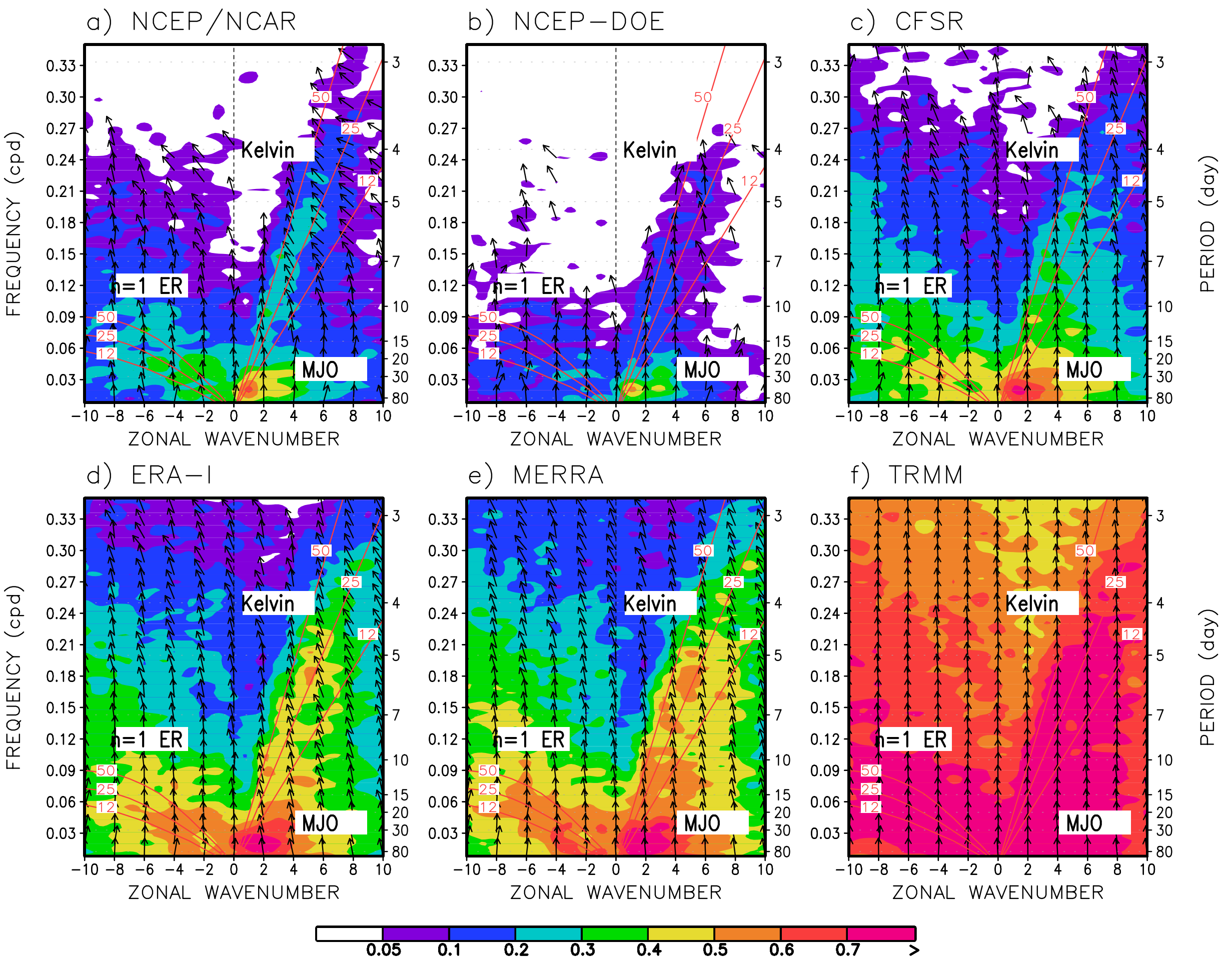

Figure 14. Coherence squared (colors) and phase lag (vectors) between GPCP precipitation and precipitation from a) NCEP/NCAR, b) NCEP-DOE, c) CFSR, d) ERA-I, e) MERRA, and f) TRMM. The symmetric spectrum is shown. Spectra were computed at individual latitude, and then averaged over 15°S–15°N. Computations are conducted using data in all seasons on 256-day segments, overlapping by 206 days. Vectors represent the phase by which reanalysis precipitation lags GPCP, increasing in the clockwise direction. A phase of 0° is represented by a vector directed upward.

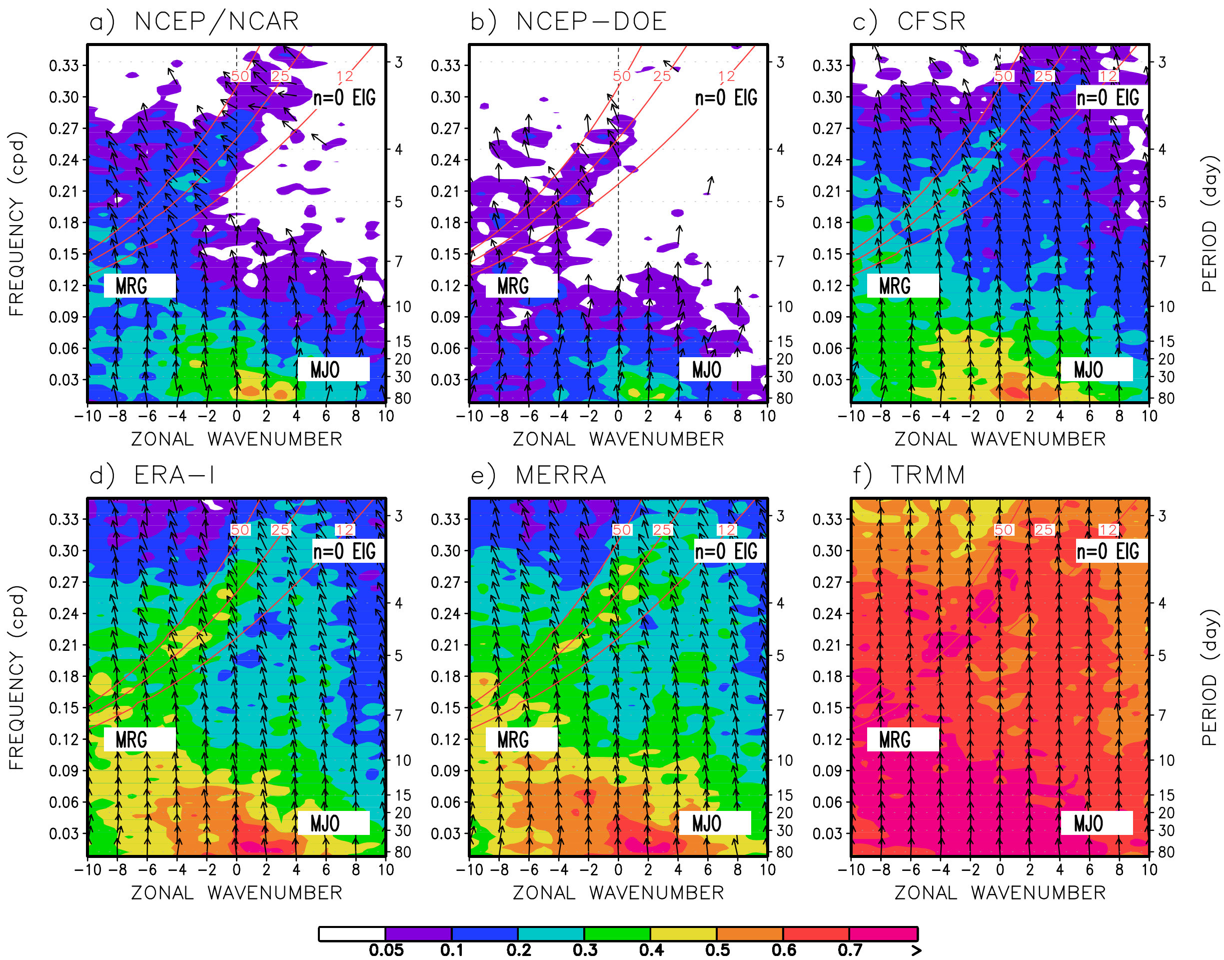

Figure 15. Same as Figure 14, except for antisymmetric spectra.

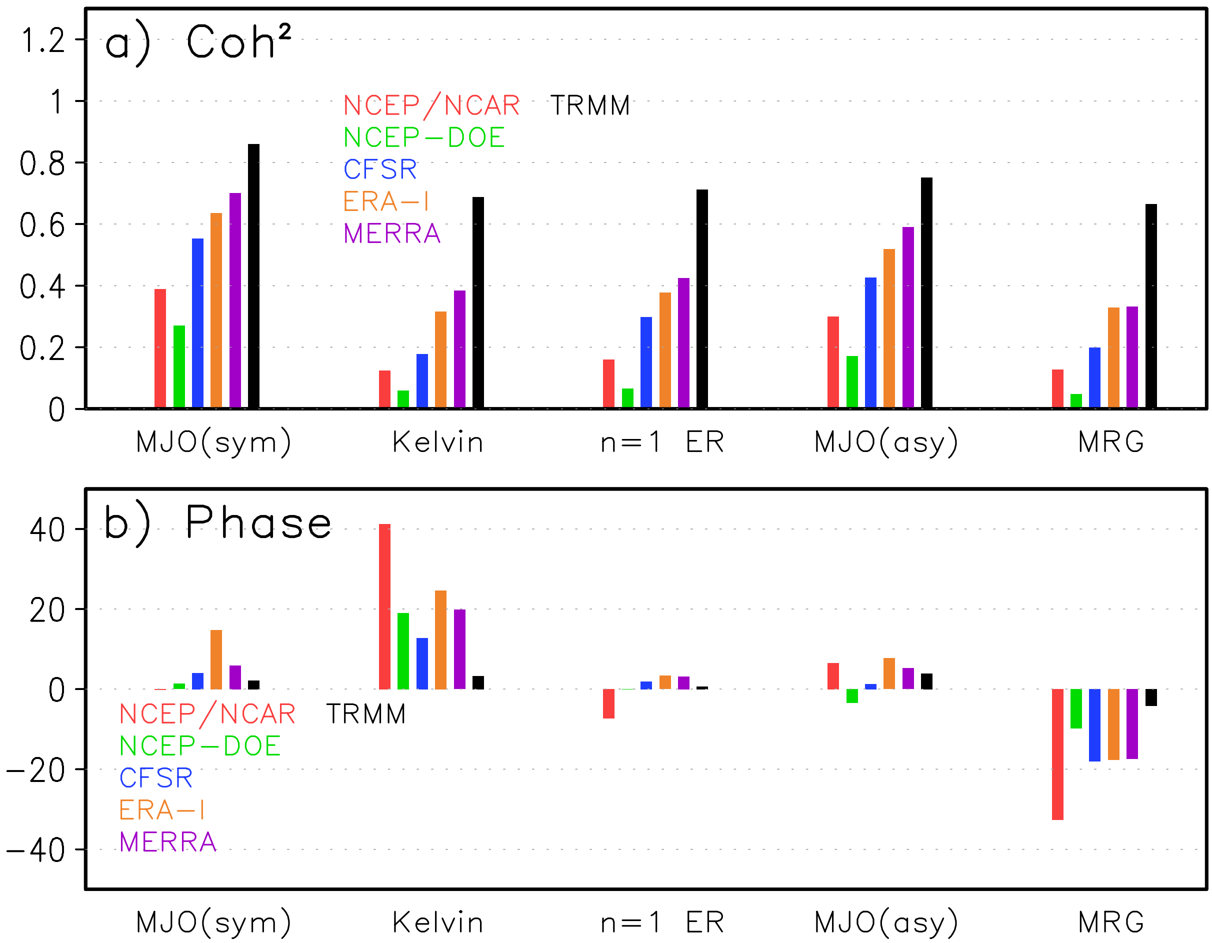

Figure 16. a) Coherence squared and b) the phase (deg) averaged for the waves from Figure 14 and 15.